INTERNATIONAL JOURNAL FOR NUMERICAL METHODS IN ENGINEERING
Int. J. Numer. Meth. Engng 2010; **81**:48–71
Published online 10 August 2009 in Wiley InterScience (www.interscience.wiley.com). DOI: 10.1002/nme.2670

Immersed particle method for fluid–structure interaction

Timon Rabczuk[1], Robert Gracie[2], Jeong-Hoon Song[3] and Ted Belytschko[3,*,†,‡]

[1]*Department of Civil Engineering, Bauhaus University Weimar, Weimar, Germany*
[2]*Department of Civil and Environmental Engineering, University of Waterloo, 200 University Avenue, Waterloo, ON, Canada*
[3]*Department of Mechanical Engineering Northwestern University, 2145 Sheridan Road, Evanston, IL 60208-3111, U.S.A.*

SUMMARY

A method for treating fluid–structure interaction of fracturing structures under impulsive loads is described. The coupling method is simple and does not require any modifications when the structure fails and allows fluid to flow through openings between crack surfaces. Both the fluid and the structure are treated by meshfree methods. For the structure, a Kirchhoff–Love shell theory is adopted and the cracks are treated by introducing either discrete (cracking particle method) or continuous (partition of unity-based method) discontinuities into the approximation. Coupling is realized by a master–slave scheme where the structure is slave to the fluid. The method is aimed at problems with high-pressure and low-velocity fluids, and is illustrated by the simulation of three problems involving fracturing cylindrical shells coupled with fluids. Copyright © 2009 John Wiley & Sons, Ltd.

Received 24 March 2009; Revised 29 April 2009; Accepted 6 May 2009

KEY WORDS: fluid–structure interaction; meshfree method; dynamic fracture

1. INTRODUCTION

An important class of problems in safety and security is that of structures impulsively loaded with sufficiently high pressures so that fracture occurs. Such structures may be either loaded by a gas or immersed in a fluid. Here, we develop a method for the modeling of fracturing structures immersed in a fluid or containing a fluid.

The paper is called an immersed particle method because it treats both the fluid and the structure by meshfree particle methods, although extension to finite element models of the structure should be straightforward. The method is a Lagrangian method, although because of the

*Correspondence to: Ted Belytschko, Department of Mechanical Engineering Northwestern University, 2145 Sheridan Road, Evanston, IL 60208-3111, U.S.A.
†E-mail: tedbelytschko@northwestern.edu
‡Walter P. Murphy and McCormick Professor.

Contract/grant sponsor: Office of Naval Research; contract/grant numbers: N00014-08-C-0592, N00014-06-1-0505, N00014-06-1-0266

capability of meshfree methods to handle large deformations, it can handle problems with very large deformations and large motions of the fluid.

The key attraction of the meshfree method for the fluid is that it naturally treats the motion of fluid through openings that develop with the nucleation and propagation of cracks. In the immersed finite element method and other methods with Eulerian treatments of the fluid, flow through the opening crack requires that the shape of the opening be defined and passed to the fluid. Furthermore, the interaction of the flow and the structure at the crack introduces some difficult issues. In contrast, the method described here requires no modifications of the algorithm to treat the flow of fluid through the opening cracks. Thus, fluid–structure interaction (FSI) with and without cracks is handled in exactly the same manner.

FSI for particle methods was previously described by Swegle and Attaway [1]. Methods for fluid interaction with large motion of rigid bodies have been proposed by Monaghan and Gingold [2, 3] using a smooth particle hydrodynamics (SPH) method. Combescure *et al.* [4] have developed an FSI method in the SPH framework using a SPH shell formulation described in Maurel and Combescure [5]. The related work of Oñate and Idelsohn should also be mentioned [6, 7], where structures are linked to nearly incompressible fluids modeled by particle finite elements. The method has been used primarily for low-pressure events where pressure waves are not of importance. Arbitrary Lagrangian–Eulerian methods for compressible fluid–structure problems have been developed by Farhat *et al.* [8]. A method that has treated problems more similar to the ones treated here is that of Cirak and Cummings [9] and Deiterding *et al.* [10].

The immersed particle method differs from the immersed finite element method in that the fluid model is Lagrangian, but by virtue of a particle discretization [11–13], it can still model substantial motions. In some cases, reinitialization of the particles is necessary; this leads to some violation of energy conservation, but in most cases it is less than 1%.

FSI within finite element models is often implemented using a node-to-surface contact algorithm. This standard FSI algorithm consists of three steps: first, the surfaces and their normals are computed; second, a contact search for fluid nodes that may come into contact with the surface is conducted; lastly, penalty forces are applied to the fluid nodes to prevent penetration of the fluid through the surfaces. Details on the implementation can be found in almost any finite element manual [14, 15] and book [16]. This algorithm requires modifications (often in the form of a set of rules) when the structure is allowed to fracture.

The method described here is intended for the simulation of the effects of high-pressure waves on structures, including crack nucleation and propagation. Therefore, the method is formulated for explicit time-integration techniques. Some of the techniques could be adapted to incompressible flows with a change in the treatment of the fluid. The method uses a Lagrangian formulation for the fluid [17] that has been shown to be stable and does not suffer from the tensile instability noted in [18–20]. The method is very simple and can treat problems of fracturing solids in contact with fluids. These are very difficult problems and have been attempted only a few times heretofore. There are some difficulties that arise in the coupling due to the fact that the domain of influence of the fluid particles is quite indistinct, but simplified treatments described here are quite effective. In these methods, the constraints between the motion of the fluid and solid are imposed in a least-square sense.

The paper is organized as follows. In the next section we describe how the fluid and structure are coupled. In Section 3 the approximations for the motion of the fluid and the structure are defined. The derivation of the governing equations is given in Section 5. In Section 6 we give several numerical examples and in Section 7 we give our conclusions.

DOI: 10.1002/nme

2. FSI CONCEPT

We will consider FSI of thin-shell structures immersed in fluids. Initially, the fluid may be on one or both sides of the structure. The structural domain is a thin shell and is denoted by Ω^{S}; its reference configuration is denoted by Ω_0^{S}. The subscript '0' denotes a reference state, which is here considered to be the initial states for any variable. The fluid domain is denoted by Ω^{F}. The superscripts 'S' and 'F' will be used to denote quantities related to the structure and the fluid, respectively. The boundaries of the structure and fluid are denoted by Γ^{S} and Γ^{F}, respectively. They are decomposed into two mutually exclusive sets: Γ_u where displacement boundary conditions $\bar{\mathbf{u}}$ are prescribed and Γ_t where tractions $\bar{\mathbf{t}}$ are applied. The structure contains cracks Γ_{c} with cohesive tractions $\mathbf{t}^{\mathrm{coh}}$. Both the fluid and the structure are subject to a body load $\mathbf{b}$. We will denote by $\mathbf{P}^{\mathrm{F}}$ and $\mathbf{P}^{\mathrm{S}}$ the nominal stresses of the fluid and structure, respectively. The densities of the fluid and structure are denoted by ρ^{F} and ρ^{S}, respectively.

Both the fluid and the structure are discretized by the sets $\mathscr{S}^{\mathrm{S}}$ and $\mathscr{S}^{\mathrm{F}}$ of meshfree particles. The FSI constraint to be enforced is a pointwise version of the constraint

$$\mathbf{u}^{\mathrm{S}}(\mathbf{X}) = \mathbf{u}^{\mathrm{F}}(\mathbf{X}) \quad \forall \mathbf{X} \in \Omega_0^{\mathrm{S}} \tag{1}$$

where $\mathbf{u}^{\mathrm{S}}$ and $\mathbf{u}^{\mathrm{F}}$ are the displacement fields of the structure and the fluid, respectively. Constraint (1) enforces the no-slip condition.

The no-slip constraint (1) is illustrated in Figure 1. In the model shown, fluid particles have been placed at the locations of the structural particles—this is done for illustration purposes only and is not a requirement of the model. In the method described here, the fluid is allowed to flow between the surfaces of a crack. Initially, the structure is unfractured, as shown in Figure 1(a). Suppose that the structure deforms and fractures (e.g. between structure particles P and Q). Once the structure has failed, fluid particles (e.g. fluid particles $A-C$) can flow between the crack surfaces, as shown in Figure 1(b). Also, we allow the fluid particles to move along the shell; for clarity, this aspect is not included in the description of the method.

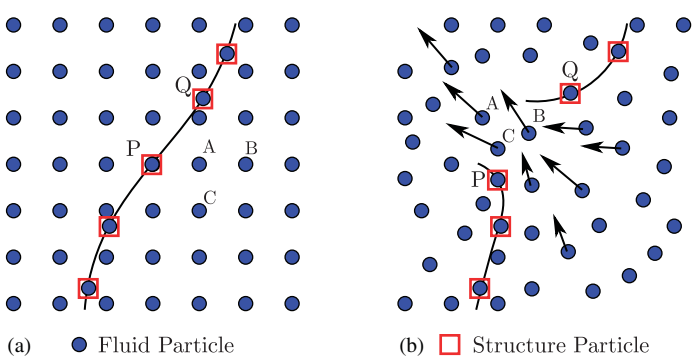

Figure 1. Illustration of the meshfree FSI model of a thin-shell structure immersed within a fluid: (a) shows the initial undeformed configuration where fluid particles have been placed at the locations of all structure particles and (b) shows the configuration of the fluid and structure particles after the structure has fractured. Fluid particles are shown to flow through the crack.

DOI: 10.1002/nme

Most FSI methods are designed for the interactions with unfractured structures and require modification to deal effectively with the case of fluid flow through a crack. The FSI method described here treats FSI within a single framework for fractured and unfractured structures alike. The details of our FSI method are given in the following sections.

3. SHELL AND FLUID DISCRETIZATION

We will consider shell structures described by a Kirchhoff–Love theory. Let the mid-surface of the structure be parameterized by two independent variables $\boldsymbol{\theta}=(\theta^1,\theta^2)$; the structure in the reference (initial) configuration is described by $\boldsymbol{\phi}_0(\boldsymbol{\theta})$, $\boldsymbol{\phi}_0\in\Re^3$. The material points in the reference configuration are given by

$$\mathbf{X}^{\mathrm{S}}(\boldsymbol{\theta})=\boldsymbol{\phi}_0^{\mathrm{S}}(\boldsymbol{\theta})+\theta^3\frac{d}{2}\,\mathbf{n}_0^{\mathrm{S}}(\boldsymbol{\theta}) \tag{2}$$

where $-1\leqslant\theta^3\leqslant 1$, d is the thickness of the shell, and $\mathbf{n}_0^{\mathrm{S}}$ is the normal to the shell at the mid-surface in the reference configuration. Latin and Greek superscripts range from 1 to 3 and from 1 to 2, respectively, and refer to quantities in the Cartesian or curvilinear coordinate systems. The current configuration is given by

$$\mathbf{x}^{\mathrm{S}}(\boldsymbol{\theta},t)=\boldsymbol{\phi}^{\mathrm{S}}(\boldsymbol{\theta},t)+\theta^3\frac{d}{2}\mathbf{n}^{\mathrm{S}}\ (\boldsymbol{\theta},t) \tag{3}$$

where t is the time, $\mathbf{n}^{\mathrm{S}}$ is the director field and $\boldsymbol{\phi}^{\mathrm{S}}$ is a point on the mid-surface in the current configuration. The Kirchhoff–Love hypothesis is imposed by requiring that $\mathbf{n}^{\mathrm{S}}$ is perpendicular to $\boldsymbol{\phi}_{,\alpha}$, $\alpha=1,2$:

$$\mathbf{n}^{\mathrm{S}}=\frac{\boldsymbol{\phi}_{,1}^{\mathrm{S}}\times\boldsymbol{\phi}_{,2}^{\mathrm{S}}}{\|\boldsymbol{\phi}_{,1}^{\mathrm{S}}\times\boldsymbol{\phi}_{,2}^{\mathrm{S}}\|} \tag{4}$$

The displacement of the mid-surface is given by

$$\mathbf{u}^{\mathrm{S}}(\boldsymbol{\theta},t)=\mathbf{x}^{\mathrm{S}}(\boldsymbol{\theta},t)-\mathbf{X}^{\mathrm{S}}(\boldsymbol{\theta},t) \tag{5}$$

We will consider fracturing structures and will model the geometry of the cracks using two level sets $f(\boldsymbol{\theta})$ and $g(\boldsymbol{\theta})$, which are defined in the tangent space of the shell structure. Level sets were first used to describe cracks in Belytschko *et al.* [21] and Stolarska *et al.* [22]. The definition of a crack by $f(\boldsymbol{\theta})$ and $g(\boldsymbol{\theta})$ is illustrated in Figure 2. The crack surface is defined by $f(\boldsymbol{\theta})=0$ and $g(\boldsymbol{\theta})<0$.

The discontinuities due to the cracks are introduced into the structure through the displacement approximation using the PU-based method of Ventura *et al.* [23] and Rabczuk *et al.* [24]. The PU-based method is the mesh-free implementation of the extended finite element method [25–27]. Let the displacement field of the shell be decomposed into a continuous part $\mathbf{u}^{\mathrm{S,C}}$ and discontinuous part $\mathbf{u}^{\mathrm{S,D}}$

$$\mathbf{u}^{\mathrm{S}}(\boldsymbol{\theta},t)=\mathbf{u}^{\mathrm{S,C}}(\boldsymbol{\theta},t)+\mathbf{u}^{\mathrm{S,D}}(\boldsymbol{\theta},t) \tag{6}$$

DOI: 10.1002/nme

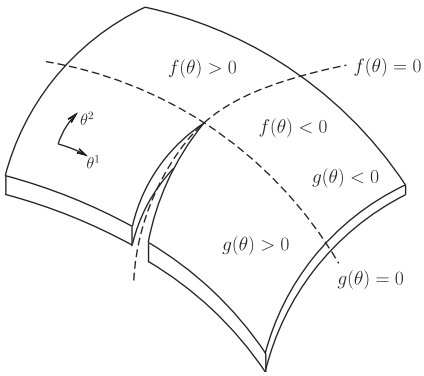

Figure 2. Description of a crack in a shell structure using level sets $f(\boldsymbol{\theta})$ and $g(\boldsymbol{\theta})$.

and

$$\mathbf{u}^{\mathrm{S,C}}(\boldsymbol{\theta}, t) = \sum_{I \in \mathscr{S}^{\mathrm{S}}} N_I^{\mathrm{S}}(\boldsymbol{\theta})\ \mathbf{u}_I^{\mathrm{S}}(t) \tag{7}$$

$$\mathbf{u}^{\mathrm{S,D}}(\boldsymbol{\theta}, t) = \sum_{I \in \mathscr{S}^{\mathrm{S}}_{\mathrm{pum}}} N_I^{\mathrm{S}}(\boldsymbol{\theta})\ H(f(\boldsymbol{\theta}))\ \mathbf{q}_I^{\mathrm{S}}(t) \tag{8}$$

where $N_I^{\mathrm{S}}(\boldsymbol{\theta})$ is the meshfree moving least squares (MLS) shape function of shell particle I [28, 29], $\mathscr{S}^{\mathrm{S}}_{\mathrm{pum}}$ is the set of particles with supports cut by the crack, $H(\cdot)$ is the Heaviside step function and $\mathbf{u}_I^{\mathrm{S}}$ and $\mathbf{q}_I^{\mathrm{S}}$ are the standard and enriched meshfree degrees of freedom associated with particle I, respectively.

We choose a quartic B-spline kernel function for the EFG shape functions, which leads to a C^2 approximation. The advantage of using a higher-order mesh-free approximation is that we can use a Kirchhoff–Love theory and only need to discretize ϕ^{S}.

We will adopt a compressible fluid model. The fluid is assumed to be inviscid, since we are concerned with high pressure, impulsive loadings where viscous effects are insignificant; it is considered to be compressible and it is described via an equation of state (EOS). We assume that the shell structure is completely immersed in the fluid and has zero thickness. Hence, when the no-slip constraint (1) is imposed, the fluid displacement field is continuous through the thickness of the shell. The displacement field of the fluid is approximated by

$$\mathbf{u}^{\mathrm{F}}(\mathbf{X}, t) = \sum_{I \in \mathscr{S}^{\mathrm{F}}} N_I^{\mathrm{F}}(\mathbf{X})\ \mathbf{u}_I^{\mathrm{F}}(t) \tag{9}$$

where $N_I^{\mathrm{F}}(\mathbf{X})$ and $\mathbf{u}_I^{\mathrm{F}}$ are the meshfree MLS shape function and degrees of freedom associated with fluid particle I, respectively.

4. CONSTITUTIVE MODEL

We used the contravariant components of the Kirchhoff stress tensor (which are identical to the components of the second Piola–Kirchhoff stress tensor in the material basis) to establish the weak

DOI: 10.1002/nme

form of the equilibrium equations for the shell model. Our shell model corresponds to a 2D theory, yielding computational savings in non-linear inelastic analysis. To take advantage of the simplicity of our previous derivations, we retain the curvilinear coordinates in the inelastic range. We use a 2D model for the radial return and rotate so that the 3-3 component corresponds to the normal. More details are given, in [24, 30, 31].

We use the Rankine criterion and a strain-based fracture criteria, see [32] for details. Therefore, cracks are initiated or propagated once the maximum principal stress or the effective plastic strain exceeds a certain threshold. Note that the corresponding quantities are averaged. We employ initially rigid linear and exponential cohesive laws [32, 33]. The exponential cohesive law is given by

$$\sigma_n = \frac{\sigma_{\max}}{\varepsilon} \exp\left(-\frac{\sigma_{\max}}{G_{\mathrm{f}}}\varepsilon\right) u_n \tag{10}$$

where $\sigma_{\max}$ is the maximum cohesive stress, G_{f} is the fracture energy and $\varepsilon = \underbrace{\max}_{\text{history}} u_n$ denotes an internal variable. A penalty term is employed to attenuate crack face interpenetration.

5. EQUATIONS OF COUPLED SYSTEM

The discrete equations governing the FSI model are obtain from the principle of virtual work: find $\mathbf{u}^{\mathrm{F}} \in \mathscr{U}^{\mathrm{F}}$ and $\mathbf{x}^{\mathrm{S}} \in \mathscr{U}^{\mathrm{S}}$ such that

$$\begin{aligned}
&\int_{\Omega_0^{\mathrm{F}}} \delta u_{i,j}^{\mathrm{F}} P_{ji}^{\mathrm{F}} \,\mathrm{d}\Omega_0^{\mathrm{F}} + \int_{\Omega_0^{\mathrm{F}}} \delta u_i^{\mathrm{F}} \rho_0^{\mathrm{F}} \ddot{u}_i^{\mathrm{F}} \,\mathrm{d}\Omega_0^{\mathrm{F}} - \int_{\Gamma_{0t}^{\mathrm{F}}} \delta u_i^{\mathrm{F}} \bar{\mathbf{t}}^{\mathrm{F}} \,\mathrm{d}\Gamma_0^{\mathrm{F}} \\
&\quad + \int_{\Omega_0^{\mathrm{S}}} \delta F_{ij}^{\mathrm{S}} P_{ji}^{\mathrm{S}} \,\mathrm{d}\Omega_0^{\mathrm{S}} + \int_{\Omega_0^{\mathrm{S}}} \delta x_i^{\mathrm{S}} \rho_0^{\mathrm{S}} \ddot{u}_i^{\mathrm{S}} \,\mathrm{d}\Omega_0^{\mathrm{S}} - \int_{\Gamma_{0t}^{\mathrm{S}}} \delta x_i^{\mathrm{S}} \bar{t}_i^{\mathrm{S}} \,\mathrm{d}\Gamma_0^{\mathrm{S}} \\
&\quad - \int_{\Gamma_{0c}} \delta x_i^{\mathrm{S}} t_i^{\mathrm{coh}} \,\mathrm{d}\Gamma_{0c} = 0 \quad \forall \delta u_i^{\mathrm{S}} \in \mathscr{U}_0^{\mathrm{S}} \quad \forall \delta u_i^{\mathrm{F}} \in \mathscr{U}_0^{\mathrm{F}}
\end{aligned} \tag{11}$$

subject to the condition (1), where

$$\mathscr{U}^{\mathrm{F}} = \{\mathbf{u} | \mathbf{u} \in \mathscr{H}^1(\Omega^{\mathrm{F}}), \mathbf{u} = \bar{\mathbf{u}}^{\mathrm{F}} \text{on } \Gamma_{0u}^{\mathrm{F}}\} \tag{12}$$

$$\mathscr{U}_0^{\mathrm{F}} = \{\delta\mathbf{u} | \delta\mathbf{u} \in \mathscr{H}^1(\Omega^{\mathrm{F}}), \delta\mathbf{u} = 0 \text{ on } \Gamma_{0u}^{\mathrm{F}}\} \tag{13}$$

$$\mathscr{U}^{\mathrm{S}} = \{\mathbf{u} | \mathbf{u} \in \mathscr{H}^2(\Omega^{\mathrm{S}}), \mathbf{u} \text{ is discontinuous on } \Gamma_{0c},\ \mathbf{u} = \bar{\mathbf{u}}^{\mathrm{S}} \text{ on } \Gamma_{0u}^{\mathrm{S}}\} \tag{14}$$

$$\mathscr{U}_0^{\mathrm{S}} = \{\delta\mathbf{u} | \delta\mathbf{u} \in \mathscr{H}^2(\Omega^{\mathrm{S}}), \delta\mathbf{u} \text{ is discontinuous on } \Gamma_{0c},\ \delta\mathbf{u} = 0 \text{ on } \Gamma_{0u}^{\mathrm{S}}\} \tag{15}$$

Note that these definitions are consistent, i.e. the fluid flow can be continuous in the presence of the discontinuity in the structural motion, as can be seen approximately in the flow shown in Figure 1.

We desired to satisfy (11) under the constraint (1) using a master–slave coupling technique. In our model the structure particles are slaves to the fluid particles. This means that the displacement of the structure will be driven by the motion of the fluid particles. The structure will then in turn

DOI: 10.1002/nme

contribute to the internal, external and kinematic forces of the fluid. It is therefore necessary to express the degrees of freedom of the structure in terms to those of the fluid.

The imposition of the constraint (1) is somewhat awkward because the MLS shape functions are not interpolatory, i.e. they do not satisfy the Kronecker delta property. A good approximation to the constraint (1) can be obtained by minimizing the following norm Π with respect to $\mathbf{u}_J^{\mathrm{S}}$ and $\mathbf{q}_K^{\mathrm{S}}$:

$$\Pi = \frac{1}{2} \sum_{I \in \mathscr{S}^{\mathrm{S}}} (\mathbf{u}^{\mathrm{S}}(\boldsymbol{\theta}_I^{\mathrm{S}}) - \mathbf{u}^{\mathrm{F}}(\mathbf{X}^{\mathrm{S}}(\boldsymbol{\theta}_I^{\mathrm{S}})))^2$$

$$= \frac{1}{2} \sum_{I \in \mathscr{S}^{\mathrm{S}}} \left(\sum_{J \in \mathscr{S}^{\mathrm{S}}} N_{JI}^{\mathrm{S}} \mathbf{u}_J^{\mathrm{S}} + \sum_{K \in \mathscr{S}_{\mathrm{pum}}^{\mathrm{S}}} N_{KI}^{\mathrm{S}} H_I \mathbf{q}_K^{\mathrm{S}} - \sum_{L \in \mathscr{S}^{\mathrm{FSI}}} N_{LI}^{\mathrm{F}} \mathbf{u}_L^{\mathrm{F}} \right)^2 \tag{16}$$

where $\boldsymbol{\theta}_I^{\mathrm{S}}$ is the curvilinear coordinate of the structural particle I, $\mathscr{S}^{\mathrm{FSI}}$ is the set of all fluid particles with shape function supports containing at least one structural particle in Ω_0^{S}, $N_{JI}^{\mathrm{S}} = N_J^{\mathrm{S}}(\boldsymbol{\theta}_I^{\mathrm{S}})$, $N_{JI}^{\mathrm{F}} = N_J^{\mathrm{F}}(\mathbf{X}^{\mathrm{S}}(\boldsymbol{\theta}_I^{\mathrm{S}}))$ and $H_I = H(f(\boldsymbol{\theta}_I^{\mathrm{S}}))$.

Minimization of Π with respect to $\mathbf{u}_J^{\mathrm{S}}$ and $\mathbf{q}_K^{\mathrm{S}}$ leads to the following system of equations:

$$\begin{bmatrix} \mathbf{A}^{uu} & \mathbf{A}^{uq} \\ \mathbf{A}^{uq\top} & \mathbf{A}^{qq} \end{bmatrix} \begin{Bmatrix} \mathbf{d}_u^{\mathrm{S}} \\ \mathbf{d}_q^{\mathrm{S}} \end{Bmatrix} = \begin{bmatrix} \mathbf{D}^u \\ \mathbf{D}^q \end{bmatrix} \left\{ \mathbf{d}^{\mathrm{FSI}} \right\} \tag{17}$$

where $\mathbf{d}_u^{\mathrm{S}\top} = \{\mathbf{u}_1^{\mathrm{S}}, \mathbf{u}_2^{\mathrm{S}}, \mathbf{u}_{n^{\mathrm{S}}}^{\mathrm{S}}\}$, $\mathbf{d}_q^{\mathrm{S}\top} = \{\mathbf{q}_1^{\mathrm{S}}, \mathbf{q}_2^{\mathrm{S}}, \mathbf{q}_{m^{\mathrm{S}}}^{\mathrm{S}}\}$ and n^{S} and m^{S} are the number of particles in the sets $\mathscr{S}^{\mathrm{S}}$ and $\mathscr{S}_{\mathrm{pum}}^{\mathrm{S}}$, respectively. The vector $\mathbf{d}^{\mathrm{FSI}}$ is the vector of the degrees of freedom of the fluid particles in $\mathscr{S}^{\mathrm{FSI}}$. The matrices are

$$A_{JjKk}^{uu} = \sum_{I \in \mathscr{S}^{\mathrm{S}}} N_{JI}^{\mathrm{S}} N_{KI}^{\mathrm{S}} \delta_{jk}, \quad J, K \in \mathscr{S}^{\mathrm{S}} \tag{18}$$

$$A_{JjKk}^{uq} = \sum_{I \in \mathscr{S}^{\mathrm{S}}} N_{JI}^{\mathrm{S}} N_{KI}^{\mathrm{S}} H_I \delta_{jk}, \quad J \in \mathscr{S}^{\mathrm{S}}, \ K \in \mathscr{S}_{\mathrm{pum}}^{\mathrm{S}} \tag{19}$$

$$A_{JjKk}^{qq} = \sum_{I \in \mathscr{S}^{\mathrm{S}}} N_{JI}^{\mathrm{S}} N_{KI}^{\mathrm{S}} H_I \delta_{jk}, \quad J, K \in \mathscr{S}_{\mathrm{pum}}^{\mathrm{S}} \tag{20}$$

$$D_{JjKk}^{u} = \sum_{I \in \mathscr{S}^{\mathrm{S}}} N_{JI}^{\mathrm{S}} N_{KI}^{\mathrm{F}} \delta_{jk}, \quad J \in \mathscr{S}^{\mathrm{S}}, \ K \in \mathscr{S}^{\mathrm{FSI}} \tag{21}$$

$$D_{JjKk}^{q} = \sum_{I \in \mathscr{S}^{\mathrm{S}}} N_{JI}^{\mathrm{S}} H_I N_{KI}^{\mathrm{F}} \delta_{jk}, \quad J \in \mathscr{S}_{\mathrm{pum}}^{\mathrm{S}}, \ K \in \mathscr{S}^{\mathrm{FSI}} \tag{22}$$

By solving Equation (17), we can drive the displacements of the structure in terms of those of the fluid, i.e.

$$\mathbf{d}^{\mathrm{S}} = \mathbf{A}^{-1} \mathbf{D} \mathbf{d}^{\mathrm{FSI}} = \mathbf{T} \mathbf{d}^{\mathrm{FSI}} \tag{23}$$

DOI: 10.1002/nme

where $\mathbf{d}^{\mathrm{S}\top}=\{\mathbf{d}_u^{\mathrm{S}},\mathbf{d}_q^{\mathrm{S}}\}$, $\mathbf{T}=\mathbf{A}^{-1}\mathbf{D}$ is the coupling matrix,

$$\mathbf{A}=\begin{bmatrix}\mathbf{A}^{uu} & \mathbf{A}^{uq}\\ \mathbf{A}^{uq\top} & \mathbf{A}^{qq}\end{bmatrix} \quad \text{and} \quad \mathbf{D}=\begin{bmatrix}\mathbf{D}^{u}\\ \mathbf{D}^{q}\end{bmatrix} \tag{24}$$

For convenience we decompose $\mathbf{T}$ as

$$\begin{Bmatrix}\mathbf{d}_u^{\mathrm{S}}\\ \mathbf{d}_q^{\mathrm{S}}\end{Bmatrix}=\begin{bmatrix}\mathbf{T}^{u}\\ \mathbf{T}^{q}\end{bmatrix}\{\mathbf{d}^{\mathrm{FSI}}\} \tag{25}$$

Each of the submatrices can be diagonalized by the row–sum technique without much loss of accuracy, so this is done here. The time derivatives of $\mathbf{d}^{\mathrm{S}}$ and $\mathbf{d}^{\mathrm{F}}$ are related by the same matrix $\mathbf{T}$, i.e.

$$\dot{\mathbf{d}}^{\mathrm{S}}=\mathbf{T}\dot{\mathbf{d}}^{\mathrm{FSI}} \tag{26}$$

$$\ddot{\mathbf{d}}^{\mathrm{S}}=\mathbf{T}\ddot{\mathbf{d}}^{\mathrm{FSI}} \tag{27}$$

The discrete equations are obtained by substituting the displacement approximations (6)–(9) into (11) along with the corresponding test functions

$$\delta\mathbf{u}^{\mathrm{F}}(\mathbf{X})=\sum_{I\in\mathscr{S}^{\mathrm{F}}}N_I^{\mathrm{F}}(\mathbf{X})\delta\mathbf{u}^{\mathrm{F}} \tag{28}$$

$$\delta\mathbf{x}^{\mathrm{S}}(\boldsymbol{\theta})=\sum_{I\in\mathscr{S}^{\mathrm{S}}}N_I^{\mathrm{S}}(\boldsymbol{\theta})\ \delta\mathbf{u}_I^{\mathrm{S}}+\sum_{I\in\mathscr{S}^{\mathrm{S}}_{\mathrm{pum}}}N_I^{\mathrm{S}}(\boldsymbol{\theta})\ H(f(\boldsymbol{\theta}))\ \delta\mathbf{q}_I^{\mathrm{S}}+\theta^3\frac{d}{2}\delta\mathbf{n}(\delta\mathbf{u}_I^{\mathrm{S}},\delta\mathbf{q}_I^{\mathrm{S}}) \tag{29}$$

The above is the PU-based representation of a crack. We also used the cracking particle method [24]; see Song and Belytschko [34] for a finite element version of the method. This gives

$$\begin{aligned}&\sum_{I\in\mathscr{S}^{\mathrm{F}}}\delta u_{Ii}^{\mathrm{F}}\left(\sum_{J\in\mathscr{S}^{\mathrm{F}}}M_{IJ}^{\mathrm{F}}\ddot{u}_{Ji}^{\mathrm{F}}-f_{Ii}^{\mathrm{F,int}}+f_{Ii}^{\mathrm{F,ext}}\right)\\ &\quad+\sum_{I\in\mathscr{S}^{\mathrm{S}}}\delta u_{Ii}^{\mathrm{S}}\left(\sum_{J\in\mathscr{S}^{\mathrm{S}}}M_{IJ}^{\mathrm{S},uu}\ddot{u}_{Ji}^{\mathrm{S}}+\sum_{K\in\mathscr{S}^{\mathrm{S}}_{\mathrm{pum}}}M_{IK}^{\mathrm{S},uq}\ddot{q}_{Ki}^{\mathrm{S}}-f_{Ii}^{\mathrm{S,int}}f_{Ii}^{\mathrm{S,ext}}\right)\\ &\quad+\sum_{I\in\mathscr{S}^{\mathrm{S}}_{\mathrm{pum}}}\delta q_{Ii}^{\mathrm{S}}\left(\sum_{J\in\mathscr{S}^{\mathrm{S}}}M_{JI}^{\mathrm{S},uq}\ddot{u}_{Ji}^{\mathrm{S}}+\sum_{K\in\mathscr{S}^{\mathrm{S}}_{\mathrm{pum}}}M_{IK}^{\mathrm{S},qq}\ddot{q}_{Ki}^{\mathrm{S}}-\overline{f}_{Ii}^{\mathrm{S,int}}+\overline{f}_{Ii}^{\mathrm{S,ext}}\right)\\ &=0\quad\forall\delta u_{Ii}^{\mathrm{F}}\ \ \forall\delta u_{Ii}^{\mathrm{S}}\ \ \forall\delta q_{Ii}^{\mathrm{S}}\end{aligned} \tag{30}$$

where the mass matrix and force vectors of the fluid are

$$M_{IJ}^{\mathrm{F}}=\rho_0^{\mathrm{F}}\int_{\Omega_0^{\mathrm{F}}}N_I^{\mathrm{F}}N_J^{\mathrm{F}}\,\mathrm{d}\Omega_0^{\mathrm{F}} \tag{31}$$

$$f_{Ii}^{\mathrm{F,int}}=\int_{\Omega_0^{\mathrm{F}}}\frac{\partial N_I^{\mathrm{F}}}{\partial X_j}P_{ji}(\mathbf{u}^{\mathrm{F}})\,\mathrm{d}\Omega_0^{\mathrm{F}},\quad I\in\mathscr{S}^{\mathrm{F}} \tag{32}$$

DOI: 10.1002/nme

and

$$f_{Ii}^{\mathrm{F,ext}} = \int_{\Omega_0^{\mathrm{F}}} N_I^{\mathrm{F}} b_i \, \mathrm{d}\Omega_0^{\mathrm{F}} + \int_{\Gamma_{0t}^{\mathrm{F}}} N_I^{\mathrm{F}} \bar{t}_i \, \mathrm{d}\Gamma_0^{\mathrm{F}}, \quad I \in \mathscr{S}^{\mathrm{F}} \tag{33}$$

respectively.

The mass matrices $\mathbf{M}^{\mathrm{S},uu}$, $\mathbf{M}^{\mathrm{S},uq}$ and $\mathbf{M}^{\mathrm{S},qq}$ along with the force vectors $\mathbf{f}^{\mathrm{S,int}}$, $\mathbf{f}^{\mathrm{S,ext}}$, $\bar{\mathbf{f}}^{\mathrm{S,int}}$ and $\bar{\mathbf{f}}^{\mathrm{S,ext}}$ of the structure are defined in Rabczuk *et al.* [24].

Equation (30) can be rewritten in matrix form as

$$\boldsymbol{\delta}\mathbf{d}^{\mathrm{F}\top}(\mathbf{M}^{\mathrm{F}}\ddot{\mathbf{d}}^{\mathrm{F}} - \mathbf{f}^{\mathrm{F}}) + \boldsymbol{\delta}\mathbf{d}^{\mathrm{S}\top}(\mathbf{M}^{\mathrm{S}}\ddot{\mathbf{d}}^{\mathrm{S}} - \mathbf{f}^{\mathrm{S}}) = 0 \tag{34}$$

where

$$\mathbf{f}^{\mathrm{F}} = \mathbf{f}^{\mathrm{F,int}} - \mathbf{f}^{\mathrm{F,ext}} \tag{35}$$

$$\mathbf{f}^{\mathrm{S}} = \begin{Bmatrix} \mathbf{f}^{\mathrm{S,int}} \\ \bar{\mathbf{f}}^{\mathrm{S,int}} \end{Bmatrix} - \begin{Bmatrix} \mathbf{f}^{\mathrm{S,ext}} \\ \bar{\mathbf{f}}^{\mathrm{S,ext}} \end{Bmatrix} \tag{36}$$

and

$$\mathbf{M}^{\mathrm{S}} = \begin{bmatrix} \mathbf{M}^{\mathrm{S},uu} & \mathbf{M}^{\mathrm{S},uq} \\ \mathbf{M}^{\mathrm{S},uq\top} & \mathbf{M}^{\mathrm{S},qq} \end{bmatrix} \tag{37}$$

To introduce the master–slave coupling between the structure and the fluid we substitute (25), (27) and

$$\delta\mathbf{u}_I^{\mathrm{S}} = \sum_{J \in \mathscr{S}^{\mathrm{FSI}}} T_{IJ}^{u} \delta\mathbf{u}_J^{\mathrm{F}} \tag{38}$$

$$\delta\mathbf{q}_I^{\mathrm{S}} = \sum_{J \in \mathscr{S}^{\mathrm{FSI}}} T_{IJ}^{q} \delta\mathbf{u}_J^{\mathrm{F}} \tag{39}$$

into (34) which gives

$$\boldsymbol{\delta}\mathbf{d}^{\mathrm{F}\top}(\mathbf{M}^{\mathrm{F}}\ddot{\mathbf{d}}^{\mathrm{F}} - \mathbf{f}^{\mathrm{F}}) + \boldsymbol{\delta}\mathbf{d}^{\mathrm{FSI}\top}\mathbf{T}^{\top}(\mathbf{M}^{\mathrm{S}}\mathbf{T}\ddot{\mathbf{d}}^{\mathrm{FSI}} - \mathbf{f}^{\mathrm{S}}) = 0 \quad \forall \boldsymbol{\delta}\mathbf{d}^{\mathrm{F}} \tag{40}$$

Invoking the arbitrariness of $\delta\mathbf{d}^{\mathrm{F}}$ in Equation (40) gives the coupled semi-discrete equations:

$$(\mathbf{M}^{\mathrm{F}} + \mathbf{T}^{\top}\mathbf{M}^{\mathrm{S}}\mathbf{T})\ddot{\mathbf{d}}^{\mathrm{F}} - \mathbf{f}^{\mathrm{F}} - \mathbf{T}^{\top}\mathbf{f}^{\mathrm{S}} = 0 \tag{41}$$

where we have made use of the fact that $\boldsymbol{\delta}\mathbf{d}^{\mathrm{FSI}} \subseteq \boldsymbol{\delta}\mathbf{d}^{\mathrm{F}}$. Stress point integration as described in [17] was used; see [18, 19] for studies on this method. The equations (41) are integrated in time using the central differencing scheme. Note that the coupling forces from the structure only affect a small subset of fluid particles, $\mathscr{S}^{\mathrm{FSI}} \subset \mathscr{S}^{\mathrm{F}}$.

Since we used a Kirchhoff–Love shell theory, the displacement field for the shell must be twice-continuously differentiable, i.e. C^1, everywhere except across the crack surfaces Γ_{c}. This is easily satisfied by the mesh-free shape functions, see Rabczuk *et al.* [24] and Krysl and Belytschko [35].

We use the reinitialization of Puso *et al.* [36]. They have proposed that an updated Lagrangian kernel formulation with a reinitialization every nth time step of all quantities of the Lagrangian

DOI: 10.1002/nme

kernel to a new reference configuration and showed that this reinitialization does not impair the stability of the meshfree method and so this scheme is adopted here.

6. NUMERICAL RESULTS

In this section we give several numerical examples to demonstrate the FSI method. We use the Rankine criterion or a strain-based fracture criterion. Therefore, cracks are initiated or propagated once the maximum principal stress or the effective plastic strain exceeds a certain threshold. Note that the corresponding quantities are averaged. We employ linear and exponentially decreasing cohesive laws and a penalty term is used in order to attenuate the crack face interpenetration. More details on the cohesive model and also the constitutive model used are given in [24, 32].

6.1. Impact of air- and water-filled cylinders

We study the response of water-filled containers of different thicknesses (0.01–1.0 mm) to projectile impact and penetration, see [37] for the experimental data. In the experiments, the height to diameter ratio $h:d$ as well as the impact velocity (190–750 m/s) were varied. The containers were perforated by a projectile that enters at mid-height. The experiments revealed that the failure pattern of water-filled cylinders differs substantially from that of the empty cylinders. Only a small hole was punched into the cylinder by the projectile for empty cylinders; however, when the container is completely filled with water, a rhombic crack opening is typical, as shown in Figure 3(a). The

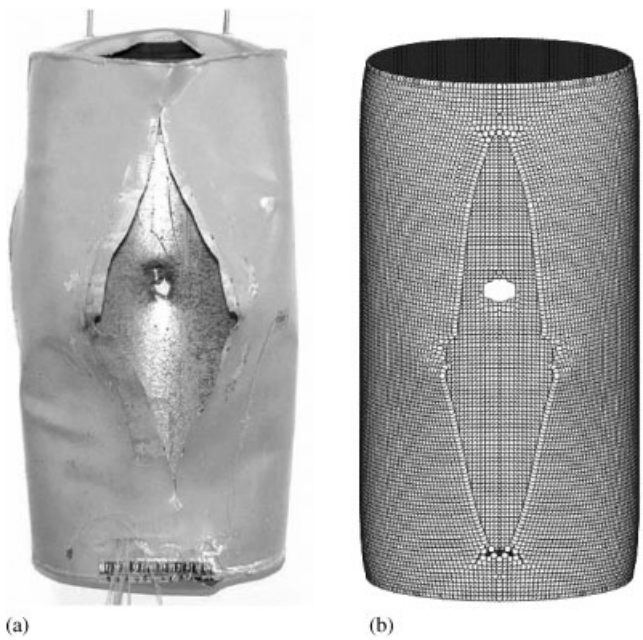

Figure 3. Final deformed shape of water-filled cylinder compared with the experimental result of Timm [37]; $h:d=2.0$ and impart velocity is 730 m/s. (a) Experiment [37] and (b) simulation result.

DOI: 10.1002/nme

vertical length of the crack depends on the thickness of the shell, the impact velocity and the ratio $h:d$ of the structure. This problem was previously investigated by a particle method with a different coupling in [24].

We have used the Johnson–Cook [38] constitutive model for the shell. The material data are given by [37]: $A=175\,\mathrm{kN/cm^2}$, $B=380\,\mathrm{kN/cm^2}$, $n=0.32$, $m=0.55$, $T_m=1538°\mathrm{C}$ and $T_r=25°\mathrm{C}$.

We first study a water-filled cylinder with a ratio $h:d=2$ ($h=600\,\mathrm{mm}$, $d=300\,\mathrm{mm}$) and thickness $t=1\,\mathrm{mm}$. The cylinder is impacted by a projectile with an initial velocity of 730 m/s. The fluid and the structure are discretized by 114 000 and 29 000 particles, respectively. The final deformed shape of the cylinder is shown in Figure 3(b) and compares well with the final experimental result shown in Figure 3(a). As can be seen, the principal failure mechanism is reproduced well. Note that the cylinder in the experiment also failed across the welds at the top and bottom. This failure mechanism was not observed in several other experiments, and was not predicted by the computation.

We next consider a water-filled cylinder with a height to diameter ratio of $h:d=2.65$. The impact velocity is 190 m/s. The impacted cylinder is shown at three different times in Figure 4. The time history of the speed of the projectile during the perforation process is shown in Figure 5(a) for two different model refinements; only a little mesh dependence is seen; hence the result for the 32 000 particle model appears to be a converged solution. The numerical simulation predicts

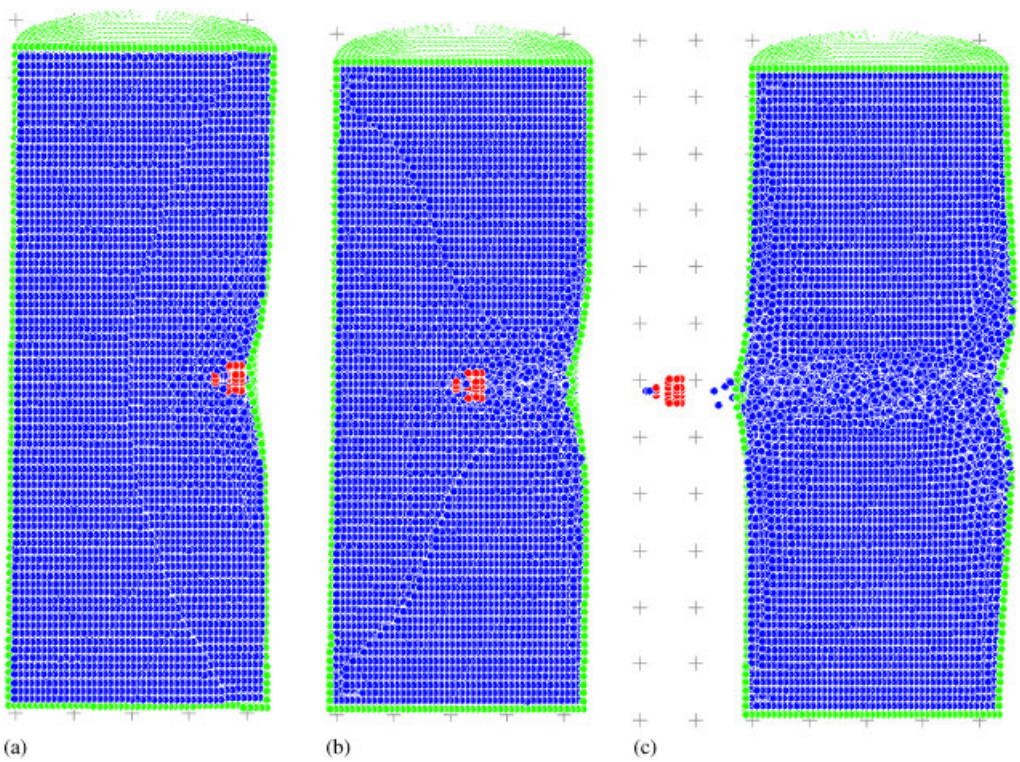

Figure 4. Deformed impacted water-filled cylinder at different time steps; $h:d=2.65$ and impart velocity is 190 m/s.

DOI: 10.1002/nme

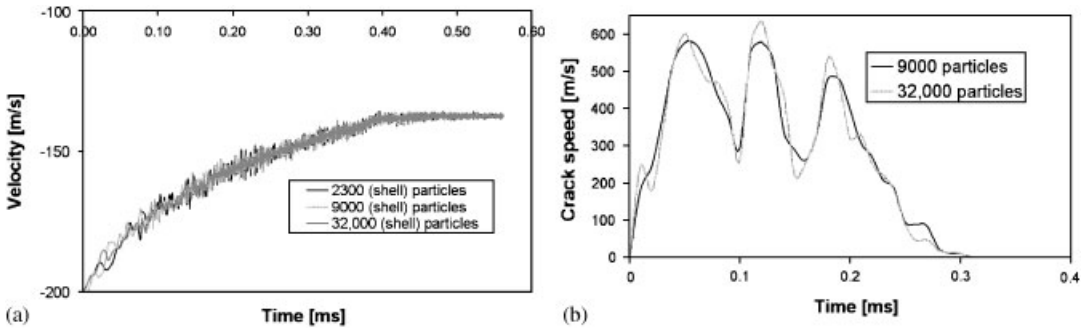

Figure 5. Time history of the velocity of the projectile and the crack speed: (a) projectile velocity and (b) crack speed.

that the impactor exits the cylinder approximately 0.4 ms after the initial impact which agrees well with the experiments. The computed exit velocity is approximately 135 m/s.

Cracking starts almost immediately after the impactor hits the cylinder. The crack speed time history for different refinements is shown in Figure 5(b). After reaching an initial peak speed at about 0.05 ms, the crack slows. Then the crack accelerates at approximately 0.1 ms and 0.18 ms when the reflecting wave hits the front of the cylinder; the dilatational wave in the water needs approximately 0.085 ms in order to travel twice the diameter of the cylinder.

Timm [37] reports the strain at five locations along the crack path, as shown Figure 6. The numerical simulations predict that the crack reaches the position of the second strain gauge at about 0.12 ms, which is a little earlier than observed experimentally. At 0.18 ms, when the second reflected wave hits the front of the cylinder, the crack has traveled approximately 7.7 cm. Cracking takes place until about 0.3 ms, at which time the impactor hits the back wall of the cylinder. After that point, the crack tip does not propagate any more, but the crack continues to open. This agrees well with observations made experimentally. Owing to the greater height to diameter ratio of this second model, the crack does not propagate through the entire length of the cylinder. The crack length is the same as for the cylinders with a height to diameter ratio of 2 which was previously described; this was also observed experimentally [37].

The final deformation and effective plastic strain of the cylindrical shell are shown in Figures 7 and 8 for two-shell discretizations with approximately 9000 and 32 000 particles, respectively. The water was modeled by 160 000 and 1 200 000 particles, respectively. Coarser discretizations of the cylinder with 2300 particles gave almost the same results.

The time history of the kinetic, cohesive and internal energies is shown in Figures 9(a)–(c). The kinetic energy decreases continuously after the impact. The cohesive energy is relatively small compared with the overall energy of the system. The error in the energy balance is shown in Figure 9(d) and is very small relative to the total energy of the system.

For empty cylinders, our computations predict a different failure pattern, as reported in [24]. Only a small hole was created in the shell at the front and back side of the cylinder. This failure mode was also observed in the experiments.

6.2. *Dynamic fracture of shells under detonation*

A series of experiments concerned with the quasi-brittle fracture of shells has been reported by Chao and Shepherd [39], and Chao [40]. These experiments involve notched thin-wall pipes filled

DOI: 10.1002/nme

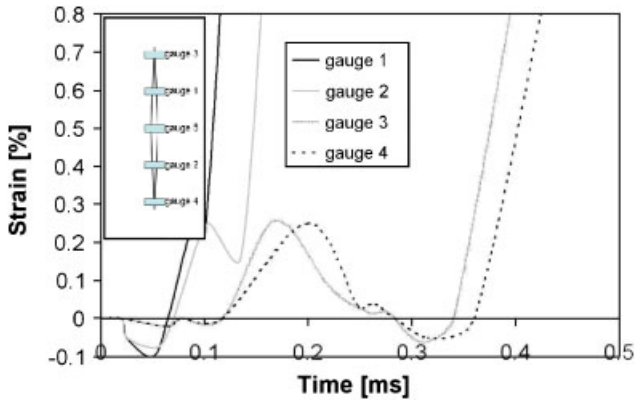

Figure 6. Strain measurement of four strain gauges used in the Timm [37] experiments. Inset shows the location of the strain gauges.

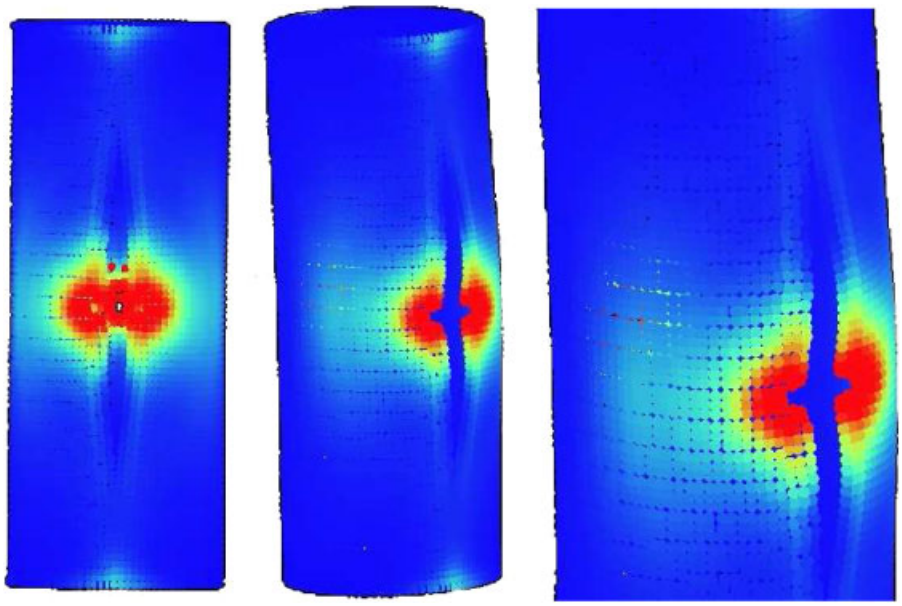

Figure 7. Final deformation and effective plastic strain of the impacted water-filled cylinder. The shell and fluid are modeled by approximately 9000 and 160 000 particles, respectively. The height to diameter ratio of the cylinder is 2.65:1.

with a gaseous explosives through which a detonation wave is passed. The wave is initiated by a detonation at the left end of the cylinder.

In this study, we focused on the numerical simulations of three experiments, shot 1 ($L=7.6$ cm), shot 7 ($L=5.08$ cm) and shot 4 ($L=2.54$ cm) [39, 40], where L is the initial notch length. They reported that with a notch size of $L=5.08$ cm, the backward crack tip, which is closer to the

DOI: 10.1002/nme

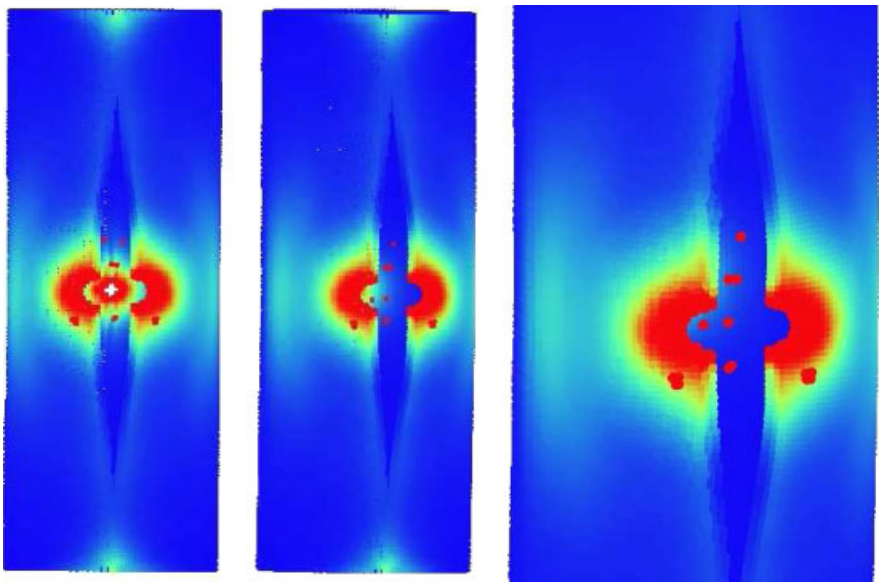

Figure 8. Final deformation and effective plastic strain for the simulation of an impact on a water-filled cylinder. The shell and fluid are modeled by approximately 32 000 and 1 200 000 particles, respectively. The height to diameter ratio of the cylinder is 2.65:1.

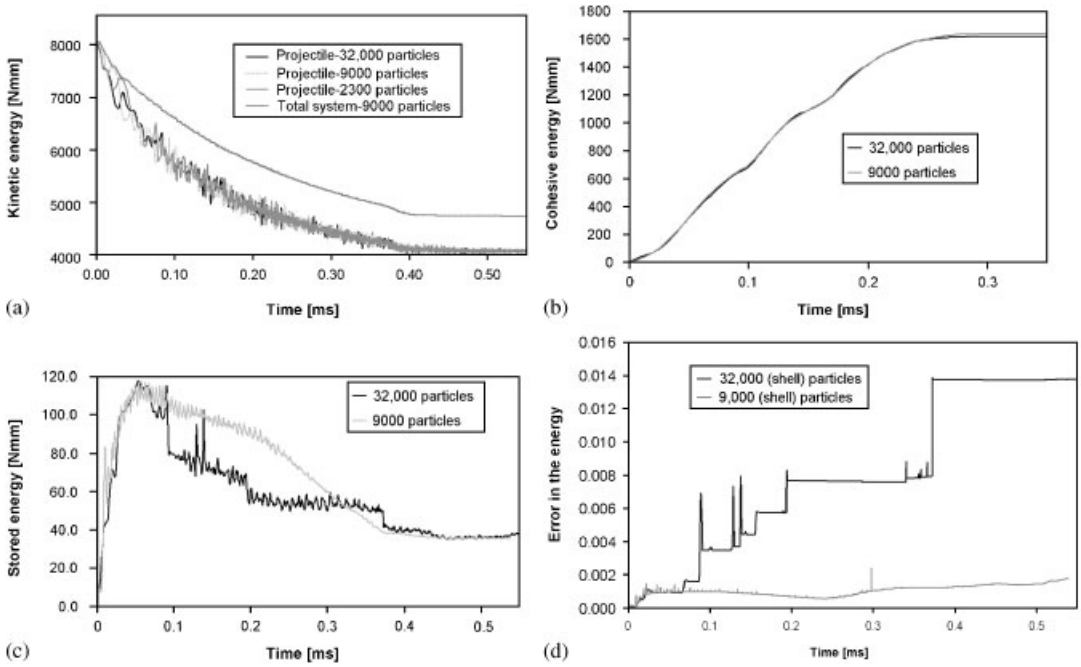

Figure 9. Time-history plots of kinetic energy, dissipated cohesive energy, stored energy and energy balance.

DOI: 10.1002/nme

detonation initiation point, showed a curved crack path, whereas the forward crack tip propagates only a short distance in a straight line and then bifurcates into two cracks. However, with a notch size of $L=2.54\,\text{cm}$, the backward crack tip curved, whereas the forward crack tip propagates only a short distance in a straight line and then is arrested. With a notch size of $L=7.6\,\text{cm}$, the tube fractures into three large pieces.

For the numerical simulations, we considered the right section of the experimental cylinder of length 91.40 cm. Models with 7000 and 28 000 structural particles were considered. The results are very similar so that we show only the results for the finest discretization. The shell material is aluminum 6061-T6, which we modeled by J_2-plasticity; density $\rho=2780.0\,\text{kg/m}^3$, Young's modulus $E=69.0\,\text{GPa}$, the Poisson ratio $\nu=0.30$ and yield stress $\sigma_y=275.0\,\text{MPa}$. We used a linear hardening law with constant slope $h_p=640.0\,\text{MPa}$. The critical strain for fracture is taken as $\varepsilon^{\max}=0.12$. After fracture, crack behavior is treated by a cohesive law with a cohesive fracture energy $G_{\text{f}}=19.0\,\text{kJ/m}^2$ (the assigned fracture energy is based on Johnson and Radon [41, 42] and Roychowdhury *et al.* [43]). The explosive gas was modeled with an equation of state (EOS) given in Beltman and Shepherd [44].

Since the densities of the explosive and the surrounding air are similar, we first considered the influence of the surrounding air as well. The air was modeled with a linear EOS. The outer radius of the air model was 350 mm, so that it takes approximately 1 ms for a wave to reach the outer boundary. At that time, cracking of the shell is completed and spurious wave reflections do not influence the results. The air did not have a significant influence on the crack pattern and therefore was not used in all computations.

In order to induce asymmetrical crack propagation of an axisymmetric shell structure and loading, we introduced a small scatter in the yield strength of the bulk material. The yield strength at every material points is perturbed by factors ranging from -5.0 to 5.0%: the perturbation factor is obtained from a log-normal distribution around the mean value of 1.0 and a standard deviation of 2.0%. We also considered bulk materials in which the yield strength is perturbed by $\pm 10.0\%$; the results are almost identical.

6.2.1. Cylinder with notch size of $L=7.6\,\text{cm}$ *(shot 1).* The deformation of the structure and pressure contours for the external fluid are shown in Figures 10 and 11. Figure 12 compares the crack pattern obtained by the numerical analysis with the experiment. We show only results of the PU-based method. The computation agrees with the major features of the crack pattern obtained in the experiment. In both cases, the pipe breaks into three pieces. On the right end, both the computation and experiment show a clean circumferential fracture. On the left end, the crack surface is more irregular. Evidently, the crack first starts at an angle and then turns to the circumferential direction. The center piece in both the experiment and computation also manifest internal cracks, but two such cracks are computed, whereas only one internal crack is apparent in the experiment.

The pressure contour in Figures 10 and 11 far from the crack is quite smooth. However, near the crack, some irregularities are apparent that may not be physical and may result from the discrete emission of fluid particles from the inside of the pipe.

6.2.2. Cylinder with notch size of $L=5.08\,\text{cm}$ *(shot 7).* Figure 13 compares the computed deformation and crack pattern for the PU-based method to the experiments. Figure 14 shows the deformed configuration of the shell for the cracking particle method. The results of the two methods are similar though the cracking particles method overestimates the crack length. Also, some short

DOI: 10.1002/nme

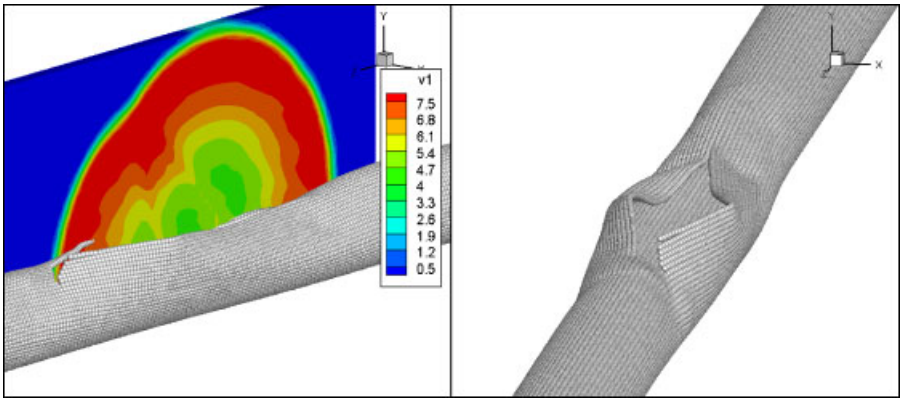

Figure 10. Simulation result with the PU-based method (shot 1) just after the crack starts to propagate. Left figure shows pressure contours in the fluid.

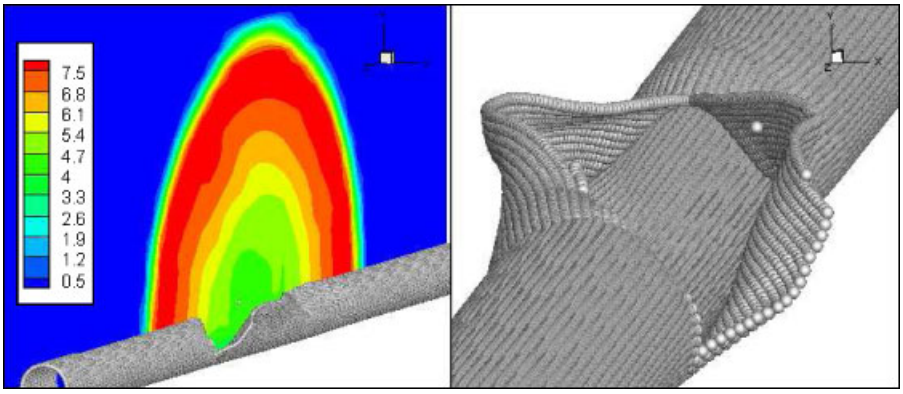

Figure 11. Simulation result with the PU-based method (shot 1) when all cracks are arrested. Left figure shows pressure contours in the fluid.

artificial cracking is evident in the cracking particle method that results at the left-hand side that was not observed for the PU-based method. We also observe that the crack on the left end turns in the opposite direction as compared with the experiment. This is not considered significant since it seems likely that the crack should be equally likely to turn in either direction. Overall, the numerical results agree well with the experiment: the crack length, the angle of crack branching and also the crack opening shape agree closely. We were also able to predict that the right-hand end of the pipe fails completely. However, the paths of the crack in the computations are smoother than in the experiment.

6.2.3. Cylinder with notch size of $L = 2.54\,\text{cm}$ *(shot 4).* Figure 15 compares the final numerical crack pattern to the experiment. The agreement is quite good. The crack in the numerical simulation curves in the same direction as obtained in the experiment. Also the turning angle, the crack length and the failure pattern agree very well with the experiment. On the left-hand side, the crack curves

DOI: 10.1002/nme

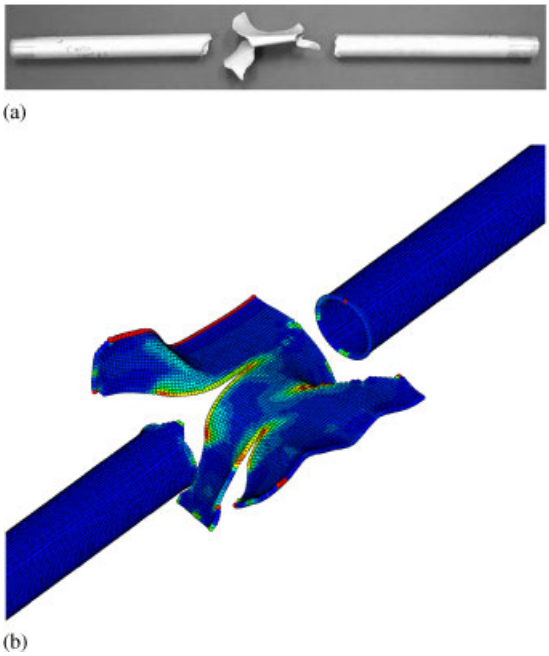

Figure 12. Final deformed shape of shell subject to explosive loading compared with the experimental results of Chao and Shepherd (shot 1) [39]. (a) Experiment [39] and (b) simulation result with the PU-based method.

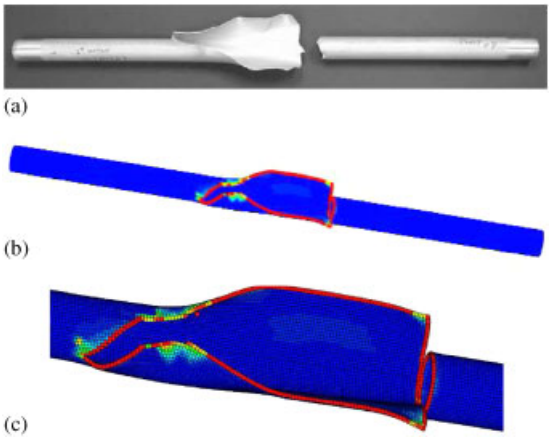

Figure 13. Final deformed shape of shell subject to explosive loading compared with the experimental results of Chao and Shepherd (shot 7) [39]. (a) Experiment [39]; (b) simulation result with the PU-based method; and (c) Simulation result with the PU-based method.

DOI: 10.1002/nme

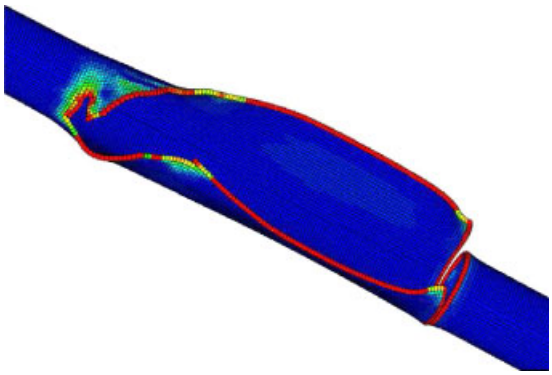

Figure 14. Simulation result with the cracking particle method (shot 7).

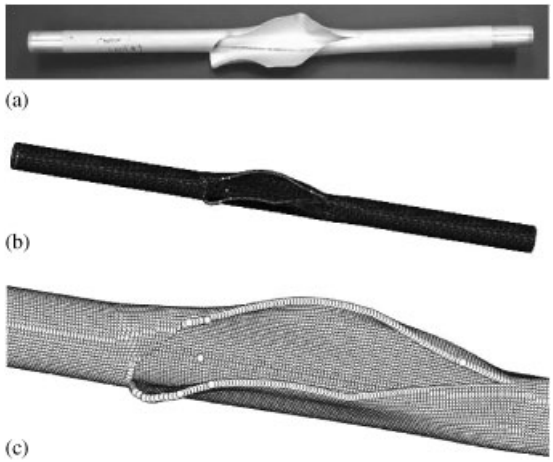

Figure 15. Final deformed shape of shell subject to explosive loading compared with the experimental result of Chao and Shepherd (shot 4) [39]. (a) Experiment [39]; (b) simulation result with the PU-based method; and (c) simulation result with the PU-based method.

downward in the circumferential direction, while on the right, the crack grows in a straight line resulting in a triangular-shaped opening. On the other hand, some of the features of the deformed shape of the experiments are absent in the computation. The upper lip is almost perfectly smooth in the computation, whereas there are several small bends in the upper lip of the specimen.

6.3. Cylinder fracture under external pressure

Consider a cylindrical shell that is immersed in water as shown in Figure 16. The thickness of the shell is 3.175 mm, the length of the cylindrical shell is 254 mm and the radius is 12.7 mm. The cylindrical shell is clamped at its ends. We assume elasto-plastic material behavior with Young's modulus $E = 71$ GPa, the Poisson ratio $\nu = 0.3$, yield strength $\sigma_Y = 207$ MPa and hardening modulus $h_p = 640.0$ MPa. Cracking is assumed to occur at an effective plastic strain of 0.12. An exponential

DOI: 10.1002/nme

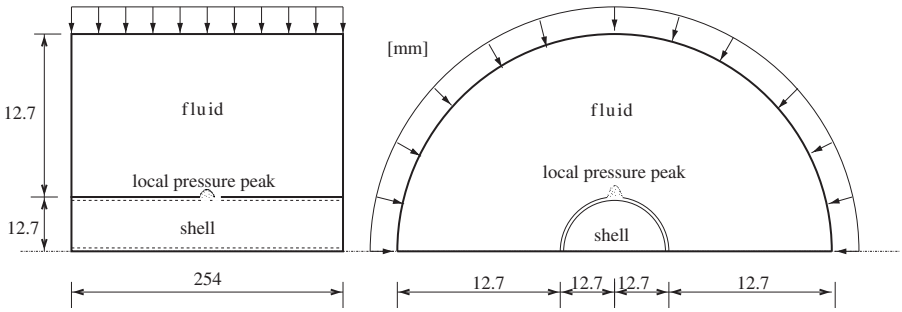

Figure 16. Initial setup of the problem: container under external water pressure (units in mm).

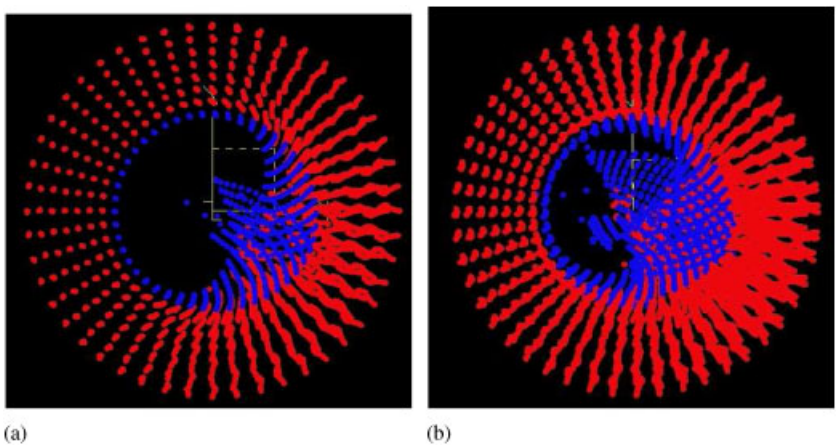

Figure 17. Deformed shape of structure and fluid with 58 000 structural particles; blue and red dots represent shell and fluid particles, respectively, in online version; in printed version, they are not distinguished. (a) Just after the onset of the failure of the structure and (b) end of simulation.

decaying cohesive law is assumed with a fracture energy $G_f = 19.0\,\mathrm{kJ/m^2}$. A 5 mm notch in the center of the cylinder was simulated by reducing the yield strength by 50%. A linearly increasing pressure was applied at the outer boundary of the water by 2 MPa/ms.

We tested different mesh refinements and will show the results for discretizations with 58 000 and 460 000 fluid particles and 7000 and 29 000 shell particles, respectively. The deformed cylindrical shell and the water entering the structure after cracking at different time steps are shown for the two discretizations in Figures 17 and 18. The deformed configuration for the 58 000 fluid particle model is shown from a different perspective in Figure 19. These figures show a cross section of the numerical results taken through the middle of the models. Figure 20 shows the deformed shell without the fluid particles; the deformation changes only slightly with refinement. The free surface of the fluid changed markedly with refinement; the amount of fluid that enters the shell increases with refinement.

The time histories of the displacements of two structural particles close to the crack in the center of the cylinder are plotted in Figure 21. It can be seen that there is barely any deformation

DOI: 10.1002/nme

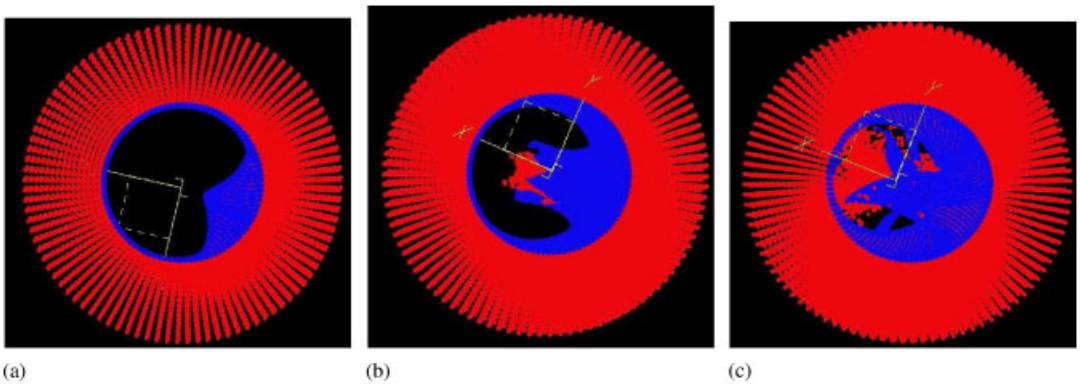

Figure 18. Deformed shape of structure and fluid with 460 000 structural particles; blue and red dots represent shell and fluid particles, respectively, in online version; in printed version, they are not distinguished. (a) Just before the onset of the failure of the structure; (b) just after the onset of the failure of the structure; and (c) end of simulation.

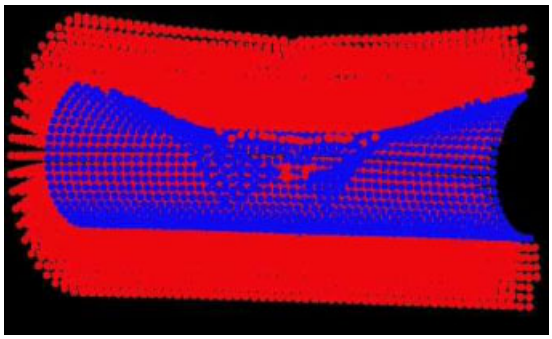

Figure 19. Longitudinal cross section of the deformed cylindrical shell surrounded by pressurized water; blue and red dots represent shell and fluid particles, respectively, in online version; in printed version, they are not distinguished.

before the onset of cracking. When the crack initiates at about 22 ms, the shell quickly deforms into its final deformed shape. The time histories of these two points are almost identical for the two discretizations.

The time history of the water pressure at two different fluid particles near the center of the crack is shown in Figure 22; the water pressure of all the other particles close to the crack is similar. After cracking at a pressure around 44 MPa, the pressure in the water drops rapidly as the water enters the structure. The pressure time histories for the two discretizations are similar.

7. CONCLUSIONS

We have described a simple immersed particle method for FSI that is able to handle complicated FSI problems including cracking and perforation with ease. We considered structures immersed

DOI: 10.1002/nme

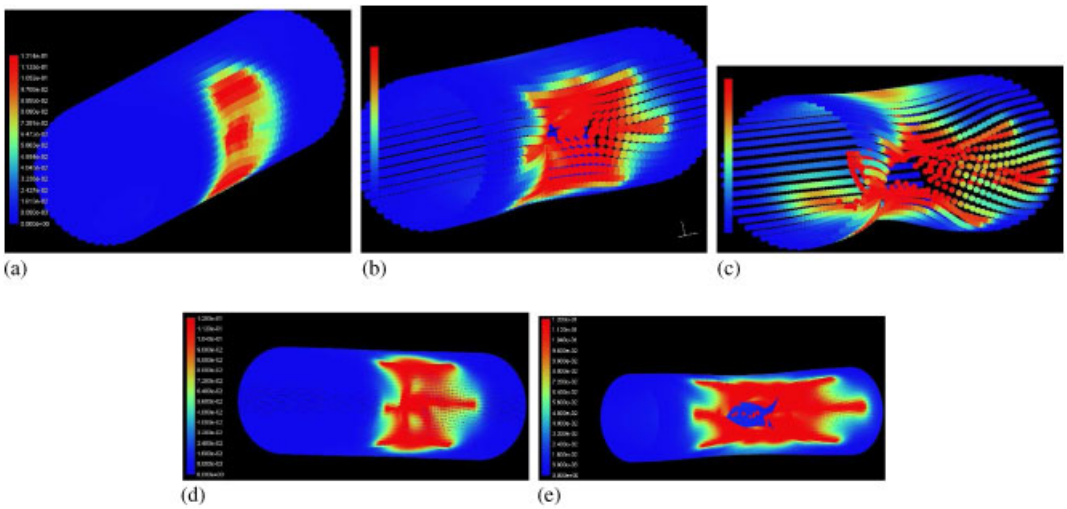

Figure 20. Deformed cylindrical shell and effective plastic strain at different times from different perspectives: (a) 7000 structural particles; (b) 7000 structural particles; (c) 7000 structural particles; (d) 29 000 structural particles; and (e) 29 000 structural particles.

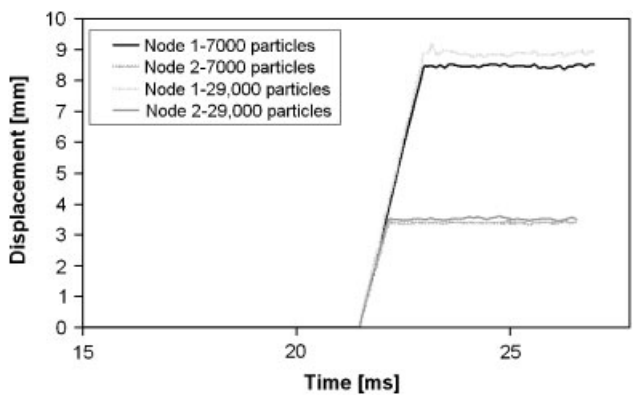

Figure 21. Displacement time history close to the crack for two different structure discretizations.

in fluids. Both the fluid and the structure are modeled by Lagrangian kernels. For very large deformation problems, the fluid is reinitialized to stabilize the Lagrangian kernel. Fracturing of the structure is modeled using either the cracking particle method or by a local partition-of-unity method. The FSI method described does not require complicated contact algorithms as contact is realized with a master–slave coupling scheme. Additional fluid particles are placed at the location of the structural particles and the structure particles are slaved to the fluid particles in the vicinity of the structure.

We modeled fracture of water-filled cylindrical shells under high-velocity impact loading, such as those studied in experiments by Timm [37]. The deformed shape of the cylinder, the crack path and speed agrees well with the experimental results. We also studied cylindrical shells under

DOI: 10.1002/nme

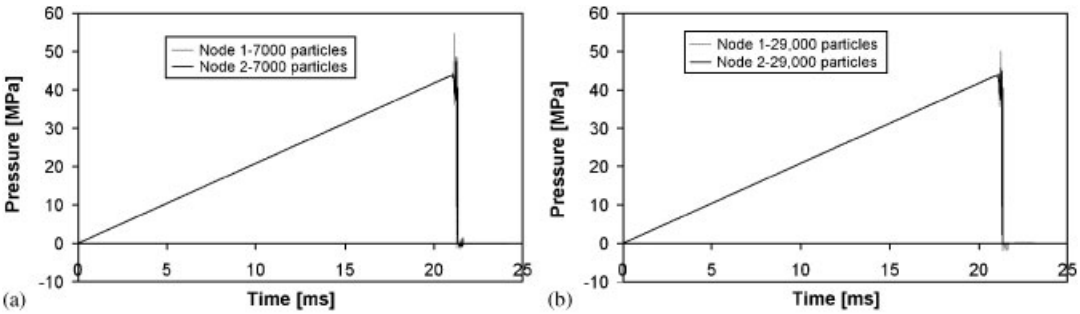

Figure 22. Fluid pressure time history close to the crack for two different fluid discretizations: (a) 58 000 fluid particles and (b) 460 000 fluid particles.

external pressure loading. These simulations demonstrate the ability of the FSI method to model scenarios where the structure cracks and fluid flows through the crack opening. Cylindrical tubes under detonation loading, such as those experimentally studied by Chao and Shepherd [39], and Chao [40], were studied as well. The numerical simulations quite well predict the various crack paths seen in the experiments, including crack branching. We found that the influence of the air surrounding the cylindrical tubes has only a minor influence on the crack patterns.

The key capability of this method is that the fluid-flow through cracks is seamlessly handled because of the properties of the master–slave contact scheme and because fracture is modeled by enrichment. The method is easy to implement, accurate and will be beneficial for FSI applications in the medium to high-pressure range.

ACKNOWLEDGEMENTS

The support of the Office of Naval Research under grants N00014-08-C-0592, N00014-06-1-0505, and N00014-06-1-0266 is gratefully acknowledged.

REFERENCES

1. Swegle LW, Attaway SW. On the feasibility of using smoothed particle hydrodynamics for underwater explosion calculations. *Computational Mechanics* 1995; **17**(3):151–168.
2. Gingold RA, Monaghan JJ. Smoothed particle hydrodynamics: theory and application to non-spherical stars. *Monthly Notices of the Royal Astronomical Society* 1977; **181**(1):375–389.
3. Monaghan JJ. An introduction to SPH. *Computer Physics Communications* 1988; **48**(1):89–96.
4. Combescure A, Maurel B, Potapov S. Modeling dynamic fracture of thin shells filled with fluid: a fully SPH model. *Mecanique and Industries* 2008; **9**:167–174.
5. Maurel B, Combescure A. An SPH shell formulation for plasticity and fracture analysis in explicit dynamic. *International Journal for Numerical Methods in Engineering* 2008; **76**:949–971.
6. Idelsohn SR, Onate E, Del Pin F. The particle finite element method: a powerful tool to solve incompressible flows with free surfaces and breaking waves. *International Journal for Numerical Methods in Engineering* 2004; **61**:964–989.
7. Pin FD, Idelsohn S, Oñate E, Aubry R. The ALE/Lagrangian particle finite element method: a new approach to computation of free-surface flows and fluid–object interactions. *Computers and Fluids* 2007; **36**(1):27–38.
8. Farhat C, Geuzaine P, Brown G. Application of a three-field nonlinear fluid–structure formulation to the prediction of the aeroelastic parameters of an F-16 fighter. *Computers and Fluids* 2003; **32**:3–29.

DOI: 10.1002/nme

9. Cirak F, Cummings JC. Generic programming techniques for parallelizing and extending procedural finite element programs. *Engineering with Computers* 2008; **24**(1):1–16.
10. Deiterding R, Cirak F, Mauch SP, Meiron DI. A virtual test facility for simulating detonation-and shock-induced deformation and fracture of thin flexible shells. *International Journal for Multiscale Computational Engineering* 2007; **5**(1):47–63.
11. Peskin CS. The immersed boundary method. *Acta Numerica* 2002; **11**:479–517.
12. Liu Y, Liu WK, Belytschko T, Patankar N, To AC, Kopacz A, Chung JH. Immersed electrokinetic finite element method. *International Journal for Numerical Methods in Engineering* 2007; **71**:379–405.
13. Wang H-W, Chessa J, Liu WK, Belytschko T. The immersed/fictitious element method for fluid–structure interaction: volumetric consistency, compressibility and thin members. *International Journal for Numerical Methods in Engineering* 2008; **74**(1):32.
14. Benson DJ. Computational methods in Lagrangian and Eulerian hydrocodes. *Computer Methods in Applied Mechanics and Engineering* 1992; **99**:235–394.
15. ABAQUS. *Theory Manual Version 6.4*. Hibbit, Karlsson and Sorensen Inc.: Providence, RI, 2004.
16. Belytschko T, Liu WK, Moran B. *Nonlinear Finite Elements for Continua and Structures*. Wiley: Chichester, 2000.
17. Rabczuk T, Belytschko T, Xiao SP. Stable particle methods based on Lagrangian kernels. *Computer Methods in Applied Mechanics and Engineering* 2004; **193**:1035–1063.
18. Swegle JW, Hicks DL, Attaway SW. Smoothed particle hydrodynamics stability analysis. *Journal of Computational Physics* 1995; **116**:123–134.
19. Belytschko T, Guo Y, Liu WK, Xiao SP. A unified stability analysis of meshless particle methods. *International Journal for Numerical Methods in Engineering* 2000; **48**:1359–1400.
20. Fries TP, Belytschko T. Convergence and stabilization of stress-point integration in mesh-free and particle methods. *International Journal for Numerical Methods in Engineering* 2008; **74**:1067–1087.
21. Belytschko T, Moës N, Usui S, Parimi C. Arbitrary discontinuities in finite elements. *International Journal for Numerical Methods in Engineering* 2001; **50**(4):993–1013.
22. Stolarska M, Chopp DL, Moës N, Belytschko T. Modelling crack growth by level sets in the extended finite element method. *International Journal for Numerical Methods in Engineering* 2001; **51**:943–960.
23. Ventura G, Xu J, Belytschko T. A vector level set method and new discontinuity approximations for crack growth by efg. *International Journal for Numerical Methods in Engineering* 2002; **54**(6):923–944.
24. Rabczuk T, Areias PMA, Belytschko T. A mesh-free thin shell for non-linear dynamic fracture. *International Journal for Numerical Methods in Engineering* 2007; **72**(5):524–548.
25. Belytschko T, Black T. Elastic crack growth in finite elements with minimal remeshing. *International Journal for Numerical Methods in Engineering* 1999; **45**(5):601–620.
26. Moës N, Dolbow J, Belytschko T. A finite element method for crack growth without remeshing. *International Journal for Numerical Methods in Engineering* 1999; **46**(1):133–150.
27. Song JH, Wang H, Belytschko T. A comparative study on finite element methods for dynamic fracture. *Computational Mechanics* 2008; **42**:239–250.
28. Belytschko T, Lu YY, Gu L. Element-free Galerkin methods. *International Journal for Numerical Methods in Engineering* 1994; **37**:229–256.
29. Belytschko T, Tabbara M. Dynamic fracture using element-free Galerkin methods. *International Journal for Numerical Methods in Engineering* 1996; **39**(6):923–938.
30. Rabczuk T, Areias P. A meshfree thin shell for arbitrary evolving cracks based on an external enrichment. *Computer Modeling in Engineering and Sciences* 2006; **16**(2):115–130.
31. Areias PMA, Song JH, Belytschko T. Analysis of fracture in thin shells by overlapping paired elements. *International Journal for Numerical Methods in Engineering* 2006; **195**:5343–5360.
32. Song JH, Belytschko T. Dynamic fracture of shells subjected to impulsive loads. *ASME Journal of Applied Mechanics* **76**(5), DOI: 10.1115/1.3129711.
33. Song JH, Areias PMA, Belytschko T. A method for dynamic crack and shear band propagation with phantom nodes. *International Journal for Numerical Methods in Engineering* 2006; **67**(6):868–893.
34. Song JH, Belytschko T. Cracking node method for dynamic fracture with finite elements. *International Journal for Numerical Methods in Engineering* 2008; **77**:360–385.
35. Krysl P, Belytschko T. Analysis of thin shells by the element-free Galerkin method. *International Journal of Solids and Structures* 1996; **33**(20–22):3057–3078.

36. Puso MA, Chen JS, Zywicz E, Elmer W. Mesh-free and finite element nodal integration methods. *International Journal for Numerical Methods in Engineering* 2008; **74**(3):416–446.
37. Timm T. Beschuss von fluessigkeitsgefuellten Behaeltern. *Ph.D. Thesis*, University of Karlsruhe, Institut fuer Massivbau und Baustofftechnologie, 2002.
38. Johnson GR, Cook WH. A constitutive model and data for metals subjected to large strains, high strain rates, and high temperatures. *Proceedings of the 7th International Symposium on Ballistics*, The Hague, The Netherlands, 1983.
39. Chao TW, Shepherd JE. Fracture response of externally flawed cylindrical shells to internal gaseous detonation loading. *Engineering Technologies in Fluids*, *Structures and Fluid/Structure Interactions*, *ASME Pressure Vessels and Piping Conference*, Vancouver, BC, 2002; 85–98.
40. Chao TW. Gaseous detonation-driven fracture of tubes. *Ph.D. Thesis*, California Institute of Technology, 2004.
41. Johnson FA, Radon JC. Evaluation of fracture energy of aluminium alloys. *Journal of Testing and Evaluation* 1975; **3**:364–367.
42. Johnson FA, Radon JC. Fracture energy and crack tunneling. *Journal of Testing and Evaluation* 1976; **4**:209–217.
43. Roychowdhury S, Roy YDA, Dodds RH. Ductile tearing in thin aluminium panels: experiments and analyses using large displacement 3d surface cohesive elements. *Engineering Fracture Mechanics* 2002; **69**:983–1002.
44. Beltman WM, Shepherd JE. Linear elastic response of tubes to internal detonation loading. *Journal of Sound and Vibration* 2002; **252**:617–655.

DOI: 10.1002/nme